Chemical Engineering Journal 419 (2021) 129601

Contents lists available at ScienceDirect

Chemical Engineering Journal

journal homepage: www.elsevier.com/locate/cej

Enhanced energy storage properties achieved in $Na_{0.5}Bi_{0.5}TiO_3$-based ceramics via composition design and domain engineering

Da Li [a], Di Zhou [a,*], Wenyuan Liu [b], Peng-Jian Wang [a], Yan Guo [a], Xiao-Gang Yao [c], Hui-Xing Lin [c]

[a] Electronic Materials Research Laboratory, Key Laboratory of the Ministry of Education & International Center for Dielectric Research, School of Electronic and Information Engineering, Xi'an Jiaotong University, Xi'an 710049, Shaanxi, China
[b] State Key Laboratory for Strength and Vibration of Mechanical Structures, School of Aerospace Engineering, Xi'an Jiaotong University, Xi'an 710049, Shaanxi, China
[c] Key Laboratory of Inorganic Functional Material and Device, Shanghai Institute of Ceramics Chinese Academy of Sciences, Shanghai 200050, China

ARTICLE INFO

Keywords:
Dielectric ceramics
Energy density
$Na_{0.5}Bi_{0.5}TiO_3$
Power density
Domain engineering

ABSTRACT

Dielectric ceramic materials with high power density and fast charge–discharge speed have attracted increasing attention in recent years. However, their mutually restricted energy density and efficiency as well as unsatisfactory temperature stability have been the main obstacles for their practical applications. Herein, a high recoverable energy density of 5.02 J·cm^{-3} and a high efficiency of ~ 90% can be obtained under 422 kV·cm^{-1} in the $Sr_{0.85}Sm_{0.1}TiO_3$ (SST)-modified $Na_{0.5}Bi_{0.5}TiO_3$ (NBT) ceramics via composition design and domain engineering strategy, and the excellent stability of energy storage properties in frequency (1–100 Hz) and temperature (20–180 °C) were also observed at 250 kV·cm^{-1} in the 0.50NBT-0.50SST ceramics, which are attributed to the improved breakdown strength (E_b) and the enhanced relaxation behavior. The increased band gap width and refined grain size are responsible for the significantly enhanced E_b of $Na_{0.5}Bi_{0.5}TiO_3$-based solid solution, being confirmed by ultraviolet and visible (UV–vis) absorption spectra as well as scanning electron microscopy. The generation of polar nanoregions as demonstrated by piezoresponse force microscopy and transmission electron microscopy results in a negligible remanent polarization and thermally stable polarization-field response. It is worth noting that the energy density will be further greatly optimized due to the improvement of E_b if this ceramic composite is made into multilayer ceramic capacitor as a dielectric layer. Moreover, a large power density of 188.6 MW·cm^{-3} and a fast discharge speed of 70 ns can also be achieved in the optimized composition. The results show that the multi-scale optimization strategy is an effective way to realize excellent comprehensive energy storage performances in the $Na_{0.5}Bi_{0.5}TiO_3$ based ceramics.

1. Introduction

The increasing demand for the quality of life has stimulated the rapid development of science and technology, while the ensuing energy waste problem makes researchers have to pay more attention to the energy storage and efficient utilization [1–3]. Capacitors, which store and release electrical energy in the form of static electricity, are essential basic electronic components in electronic circuits and are widely used in coupling, tuning circuit and energy conversion. Many advanced electronic devices, such as electromagnetic devices and hybrid electric vehicles, require capacitors with both high energy and power density [4,5]. Multilayer ceramic capacitors (MLCCs) can be widely employed in high power systems because of their fast charge–discharge rate and excellent thermal stability, but possess low energy density compared with batteries [6,7]. The energy storage properties (ESP) of MLCCs needs to be enhanced to a higher level to further broaden the application, which also plays an important role for the lightweight and integration of electronic devices.

In this paper, a multiscale optimization strategy (including grain and atomic scales) was proposed to improve the ESP of dielectric capacitors. A schematic diagram of strategies for achieving excellent energy storage performance through composition design and domain engineering is given as shown in Fig. 1. First at all, on the 10^{-3} m scale: it must be understood that for MLCCs, in addition to the preparation process, the composition of dielectric layer determines the comprehensive energy storage performances of capacitors to a great extent. Thus, more attention should be paid to ceramic dielectric materials to maximize the electrical energy stored in capacitors [8]. Additionally, the total energy

* Corresponding author.
E-mail address: zhoudi1220@gmail.com (D. Zhou).

https://doi.org/10.1016/j.cej.2021.129601
Received 12 February 2021; Received in revised form 18 March 2021; Accepted 27 March 2021
Available online 6 April 2021

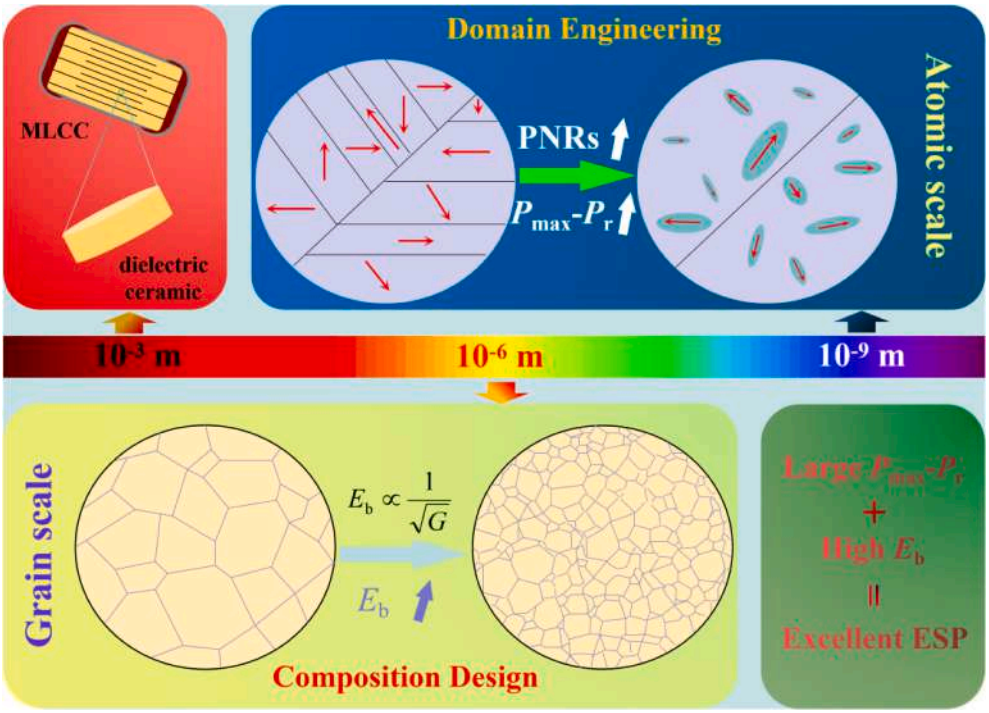

Fig. 1. Schematic diagram of the strategy for achieving excellent energy storage properties via composition design and domain engineering.

density (W_t), recoverable energy density (W_{rec}) and energy efficiency (η) of dielectric ceramics can be evaluated using the Eqs(1)-(3):

$$W_t = \int_0^{P_{max}} EdP \tag{1}$$

$$W_{rec} = \int_{P_r}^{P_{max}} EdP \tag{2}$$

$$\eta = W_{rec}/W_t \times 100\% \tag{3}$$

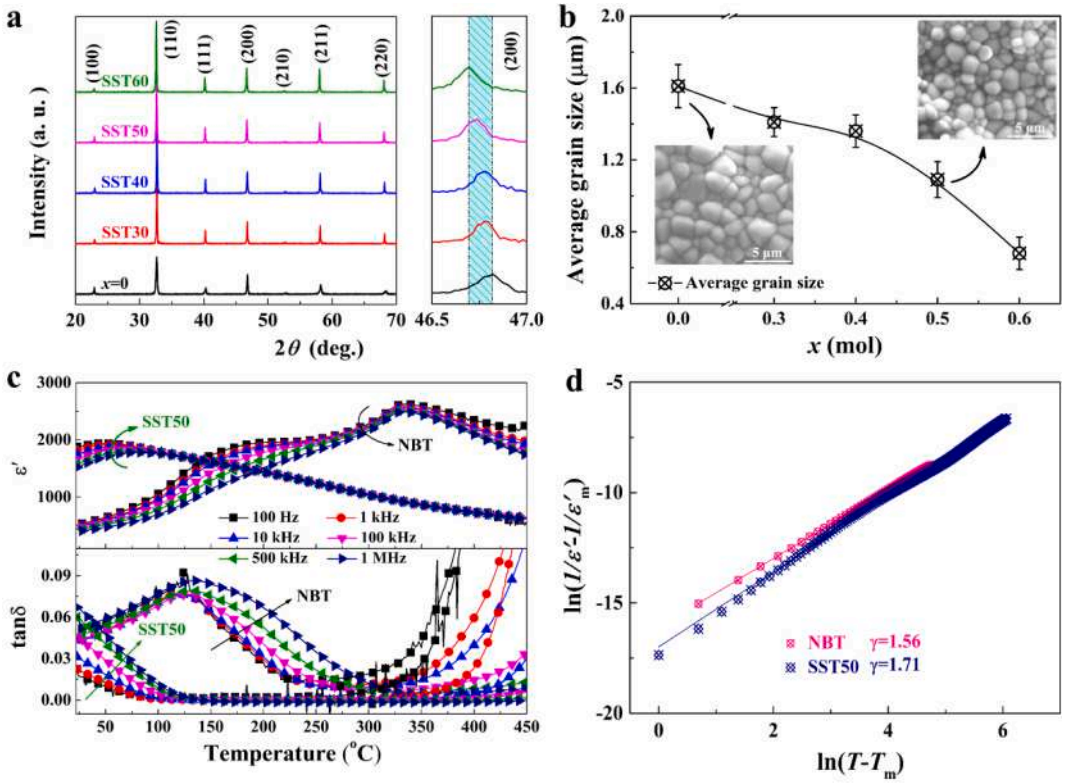

Fig. 2. (a) XRD patterns of the (1-*x*)NBT-*x*SST ceramics and the enlarged (200) peaks. (b) Average grain sizes of (1-*x*)NBT-*x*SST ceramics. Insets are the microstructures of NBT and SST50 ceramics. (c) Temperature dependence of the dielectric constant (ε') and loss (tanδ) of NBT and SST50 ceramics measured in the temperature range of 22 °C to 450 °C. (d) Plot of $\ln(1/\varepsilon'-1/\varepsilon'_m)$ as a function of $\ln(T-T_m)$ according to the modified Curie-Weiss law for the NBT and SST50 ceramics.

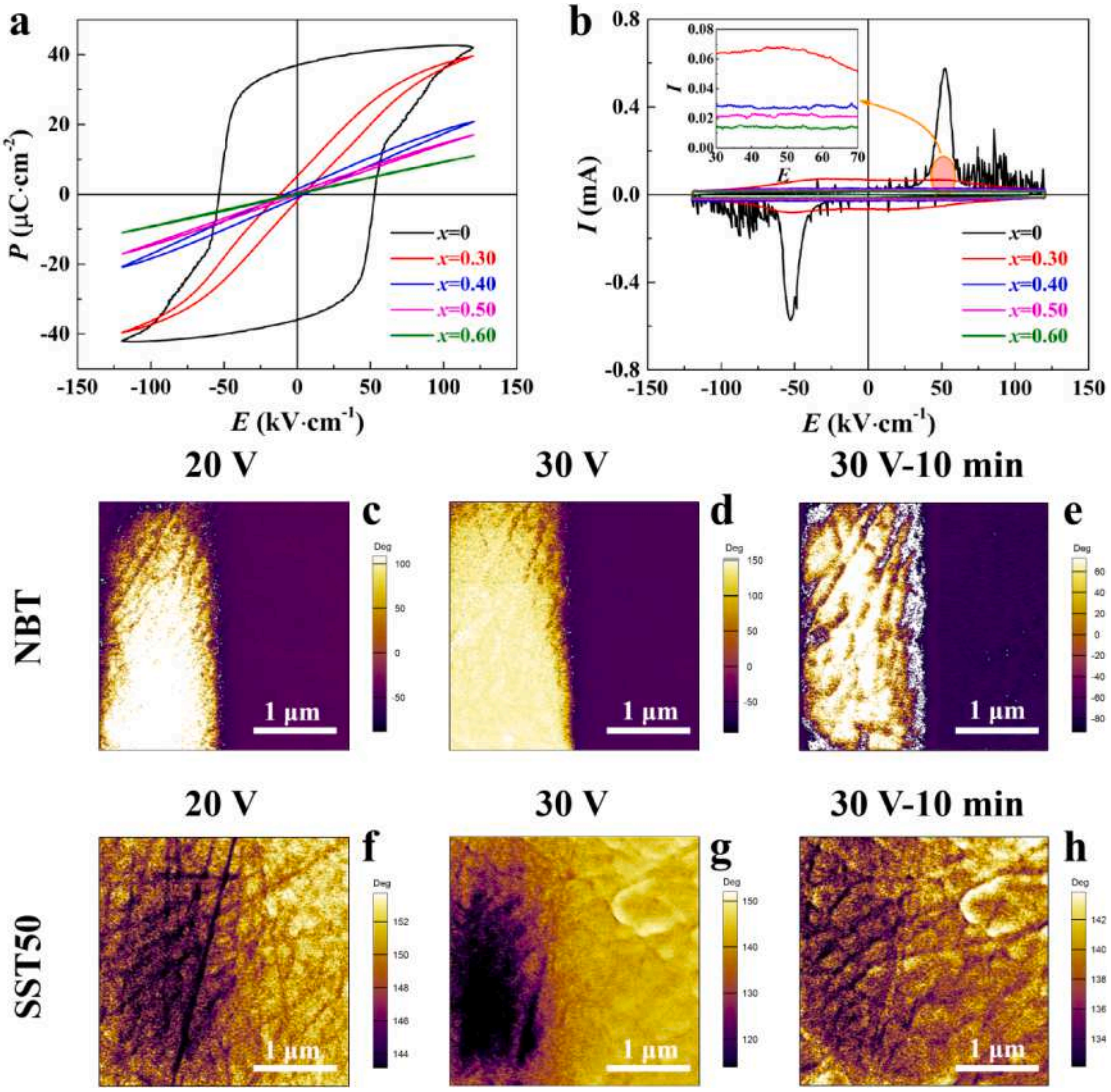

Fig. 3. (a) *P-E* hysteresis loops and (b) corresponding *I-E* curves of (1-*x*)NBT-*x*SST ceramics at 120 kV·cm^{-1}. Out-of-plane PFM phase images and domain evolution under an external electric field for pure NBT ceramics: (c) 20 V, (d) 30 V and (e) 30 V-10 min. Out-of-plane PFM phase images and domain evolution under an external electric field for SST50 ceramics: (f) 20 V, (g) 30 V and (h) 30 V-10 min.

where P means the polarization at an electric field (E), P_{max} and P_r are the maximum polarization and the remanent polarization, respectively. Therefore, for the dielectric ceramics used for energy storage, both a high breakdown field strength (E_b) and a large ΔP (P_{max}-P_r) value should be required. Among all kinds of ceramic dielectric materials, Pb-based antiferroelectric (AFE) ceramics have been widely explored due to their prominent energy storage properties, but the inevitable toxicity has become the main obstacle to their further development [9]. By contrast, $Na_{0.5}Bi_{0.5}TiO_3$ (NBT)-based ceramics are a potential and promising dielectric material due to their strong ferroelectricity and environmental friendliness, which always arouses interest in energy storage applications. For instance, Zhang et al. enhanced the W_{rec} to 2.3 J·cm^{-3} in NBT-$LiTaO_3$ ceramics, while their η value was only 74.2% [10]; Qiao et al. fabricated 0.95(0.6$Bi_{0.5}Na_{0.5}TiO_3$-0.4$Sr_{0.7}Bi_{0.2}TiO_3$)-0.05$AgNbO_3$ ceramics and obtained a high W_{rec} of 3.62 J·cm^{-3} together with high η of 86.8% [11]. Furthermore, on the 10^{-6} m scale (grain scale): the relationship between the E_b and average grain sizes (G) can be summarized as $E_b \propto 1/\sqrt{G}$. One can be found that reducing the average grain size of ceramics by composition design strategy will be beneficial to the increase of E_b value, which will greatly improve the energy density of the ceramics. More importantly, on the 10^{-9} m scale (atomic scale): the destroyed long-range polar order of FE ceramics and the induced high-dynamic and small-size polar nanoregions (PNRs) via domain engineering will lead to the enhancement of relaxation behavior of dielectric ceramics. And the emergence of PNRs makes it easier for the domain to be switched after the external electric field is removed, that is, the realization of a large P_{max} value under the action of an applied electric field and a negligible P_r value when the electric field is removed, which can significantly optimize the ESP.

Based on the above discussions, the (1-*x*)$Na_{0.5}Bi_{0.5}TiO_3$-*x*$Sr_{0.85}Sm_{0.1}TiO_3$ ((1-*x*)NBT-*x*SST) ceramics were prepared using solid-phase sintering and cold isostatic forming. Phase evolution, micromorphology, dielectric behaviors and energy storage characteristics of the NBT ceramics with SST additions were analyzed systematically. The achievement of remarkably improved E_b value (422 kV·cm^{-1}) and significantly reduced P_r value (1.48 μC·cm^{-2}) leads to an ultrahigh W_{rec} of 5.02 J·cm^{-3} and a high η of ~ 90% in the $x = 0.50$ composition, together with superior temperature stability over the range of 20 °C-180 °C. The potential reasons for improving E_b values and reducing P_r values was analyzed in detail.

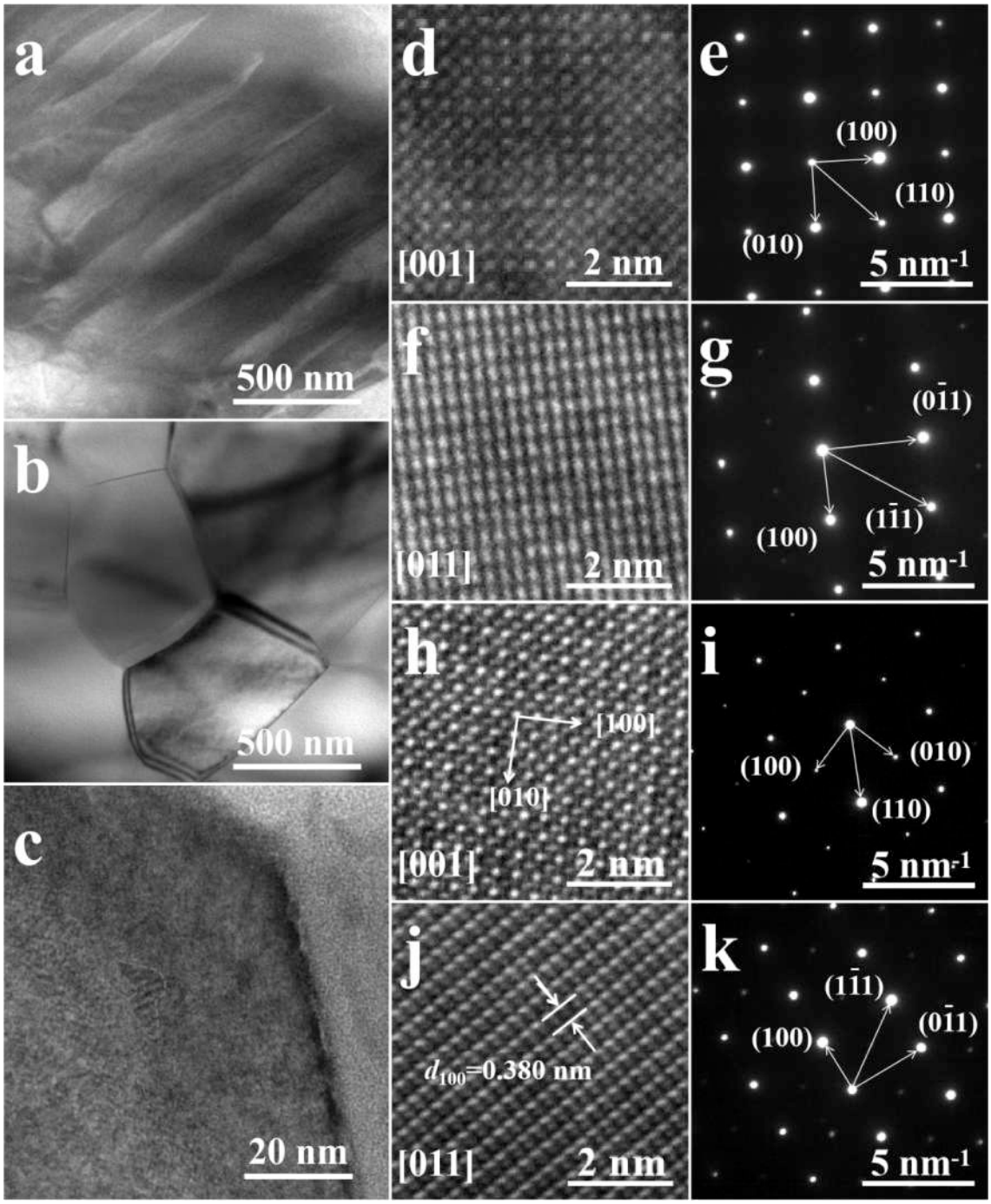

Fig. 4. (a) Domain morphology of pure NBT ceramics. (b, c) Domain morphology on different scales of SST50 ceramics. (d, f) HR-TEM images and (e, g) SAED patterns along [0 0 1]c and [1 1 0]$_C$ of pure NBT ceramics, respectively. (h, j) HR-TEM images and (i, k) SAED patterns along [0 0 1]c and [0 1 1]$_C$ of SST50 ceramics, respectively.

2. Results and discussion

Fig. 2 (a) gives the phase structure of the (1-*x*)NBT-*x*SST ceramics at room temperature. Obviously, all the materials belong to a typical perovskite structure, which suggests that SST can enter the NBT lattices without generating impurities. We can also find from the enlarged (2 0 0) peaks that, with increasing SST additions, the diffraction peaks gradually move to a lower degree, which is caused by the substitution of Sr^{2+} with a larger ionic radius at the A-site, indicating the increase of cell volume [12]. The lattice parameters and cell volume (*V*) gradually increase with the increase of SST content, as displayed in Fig. S1, which also supported the XRD analysis. Fig. S2 and Fig. 2 (b) display the micromorphology and average grain sizes of the natural surface after sintering of all ceramic samples. As shown, a dense microscopic structure with few visible pores can be observed, and the average grain size of sample monotonically decreases with the introduction of SST, and is 1.61, 1.40, 1.36, 1.09 and 0.68 μm for $\times$ = 0, 0.30, 0.40, 0.50 and 0.60 mol, respectively. Previous studies have shown that the E_b values of dielectric ceramics are linked to their grain sizes [13,14]. In dielectric ceramics, depletion regions generated by the grain boundaries can prevent charge carriers from passing through them. The density of grain boundaries increases with the decrease of grain size, resulting in more

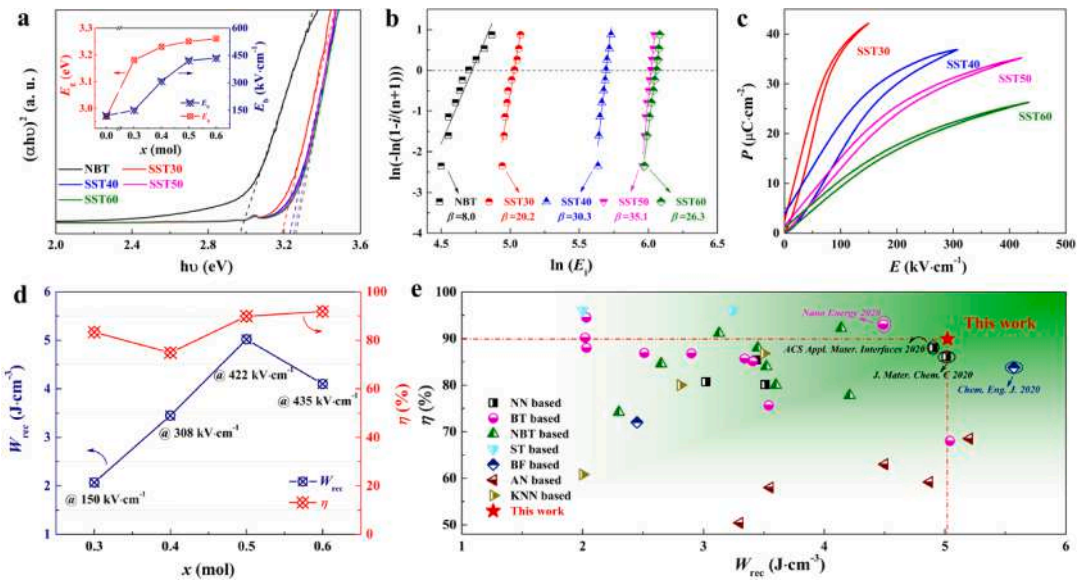

Fig. 5. (a) $(\alpha h\nu)^2$ versus hν plot of (1-x)NBT-xSST ceramics. Insets are the variation of E_g and E_b. (b) Weibull distribution of (1-x)NBT-xSST ceramics. (c) *P-E* loops and (d) Energy storage properties of (1-x)NBT-xSST ceramics under critical electric fields. (e) A comparison of W_{rec} and η values among recently reported bulk ceramics.

depletion regions, higher resistivity and larger E_b, that is, grain refinement can improve E_b [15,16].

Frequency dependent dielectric properties for all samples at toom temperature from 100 Hz to 1 MHz are presented in Fig. S3 (a). It can be found that the dielectric constant (ε') only decreased slightly and even remained stable in the whole test frequency range, which is very important for the frequency stability of dielectric materials. Moreover, at a certain measured frequency, the ε' value first increases and then decreases with the introduction of SST, and the maximum value of ε' is obtain in SST50 ceramics. The dielectric loss (tanδ) decreases with increasing of the SST content, for example at $x = 0.50$, the measured ε' values are as high as ~1870 while the values of tanδ are below 0.06 over all the measured frequency range, which is particularly important for the realization of excellent ESP. Fig. 2 (c) and Fig. S3 (b-d) show the ε' and tanδ as a function of temperature for the SST-modified NBT-based bulk ceramics at different frequencies. The results show that double abnormal peaks appear on the dielectric curves when × < 0.50 mol, similar to other BNT-based ceramics [17]. They are a low-temperature shoulder (T_s) caused by thermal relaxation of rhombohedral (R3c) and tetragonal (P4bm) structured PNRs and a broad maximum (T_m) attributed to the transition of PNRs from R3c to P4bm structure and the thermal evolution of P4bm PNRs. [18,19] With the increase of SST content, T_m moves towards a lower temperature and the maximum of ε' gradually decrease, which is because the introduction of SST increases the site disorder, breaks the original long-range FE order, and enhances the RFE properties. The relaxor behavior can also be analyzed by diffuseness degree (γ), which can be calculated through Eq. (4) [20,21].

$$\frac{1}{\varepsilon'} - \frac{1}{\varepsilon'_m} = \frac{(T - T_m)^\gamma}{C} \tag{4}$$

where ε'_m is the maximum value of the dielectric constant and C means the Curie constant. Fig. 2 (d) depicts plot of ln(1/ε'-1/ε'_m) as a function of ln(T-T_m) for the NBT and SST50 ceramics, the slope of the line fitted by all points is the diffuseness degree. As is shown, a large γ value of 1.71 is obtained in SST50 ceramics, which can also suggest a strong relaxation behavior.

Fig. 3 (a) and (b) present the bipolar *P-E* hysteresis loops and the corresponding current-electric field (*I-E*) curves of (1-x)NBT-xSST ceramics under 120 kV·cm^{-1}, respectively. Obviously, both P_r and P_{max} values decrease and the curve becomes slimer with the incorporation of SST. Additionally, the *I-E* curve of NBT ceramic possess double sharp peaks of current due to the domain inversion under coercive fields, indicating a strong FE characteristic. And no significant current peak was measured at $x = 0.30$, 0.40, 0.50 and 0.60, which confirmed the weakened ferroelectricity and enhanced ergodicity behavior with increasing SST content. In short, the modified NBT ceramics show lower polarization but enhanced linearity of the *P-E* loop, which are proposed to be linked with the size of domains and the dynamic characteristic of domains under external stimuli such as electric fields [22,23]. PFM technique is considered to be an effective tool for observing the domain response under external electric fields, which also provides nanoscale insight into FE/RFE performances [24,25]. Accordingly, PFM method was performed in the NBT and SST50 ceramics to investigate the evolution of domain responses at different voltages (20 V and 30 V) and a relaxation time of 10 min, as shown in Fig. 3 (c-h). PFM amplitude images under an external electric field for the NBT and SST50 ceramics are depicted in Fig. S4. Divide an area of 3 × 3 μm^2 evenly into two parts, a negative voltage is added to the left area and a positive voltage of the same amplitude is added to the right area. It can be found that the 180° domains can be richly induced at a low voltage of 20 V for the pure NBT ceramics (Fig. 3 (c)), which manifests macroscopically as the large P_{max} value under the low electric field. The feedback signals become more pronounced with the voltage increased to 30 V (Fig. 3 (d)), and most domains are still in the induced state (Fig. 3 (e)) after being relaxed for 10 min, which explains the large P_r value of the original NBT ceramic [26]. By contrast, extremely weak feedback signals were detected in the SST50 ceramics at the electric field of 20 V (Fig. 3 (f)), 180° domains are still not detected despite the PFM signal enhances when the voltage was increased to 30 V (Fig. 3 (g)), indicating a reduced sensitivity of the polarization to external voltage. The domains return to its original state and cannot be recognized after the relaxation for 10 min (Fig. 3 (h)), which means that SST50 ceramics possess robust relaxation properties [16]. Consequently, the substitution of SST results in the transformations of FE domain of NBT ceramics into highly-dynamic PNRs, also reveals the potential origin why SST50 ceramics have a negligible P_r [27,28].

TEM methods are the most direct way to observe domain morphology. Fig. 4 (a-c) display domain morphology of pure NBT ceramics and SST50 ceramics. Strip-like domains with a width of ~ 200 nm can be found in NBT ceramic, while such domain cannot be observed

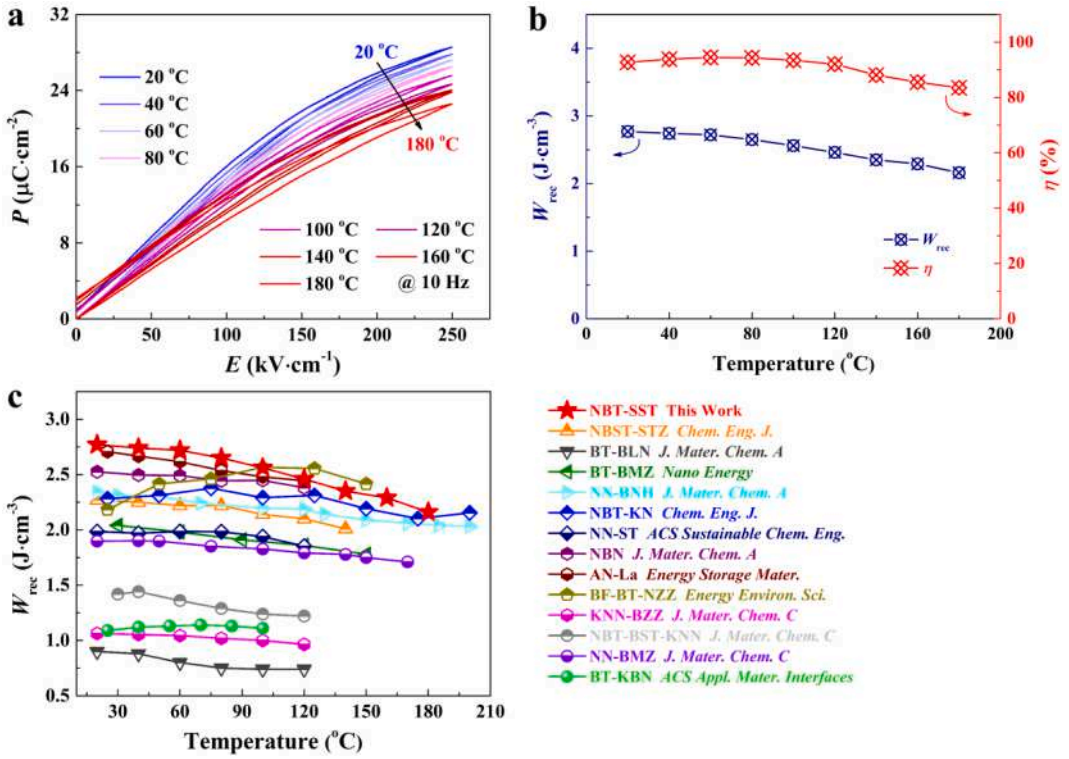

Fig. 6. (a) *P-E* hysteresis loops and (b) W_{rec} and η values of the SST50 ceramic at different temperatures from 20 °C to 180 °C at 250 kV·cm^{-1} and 10 Hz. (c) A comparison of temperature stability among the SST50 ceramic and other lead-free bulk ceramics.

in SST50 ceramics at the same scale (Fig. 4 (b)). The domain size observed in SST-doped NBT ceramics decreased dramatically to ~ 10 nm as depicted in Fig. 4 (c), which confirms the previously stated substitution of SST transforms the FE macro domain of NBT ceramics into the PNRs. The decreased domain size demonstrates a same trend with the suppressed P_r and improved energy efficiency. According to high-resolution TEM (HR-TEM) images and selected area electron diffraction (SAED) patterns along [0 0 1]c and [1 1 0]$_C$ of pure NBT and SST50 ceramics in Fig. 4(d-k), consistent with XRD results above, suggesting the good crystalline quality and periodic perovskite structure of samples. Additionally, the superlattice diffraction spots the 1/2{ooo}-type can be observed in Fig. 4g and Fig. 4k, which signifies the presence of rhombohedral *R3c* phase that induce the high polarization upon high electric fields along with pseudocubic lattice. [29–31]. In conclusion, the conversion of large-size FE domains to PNRs with both low energy barriers and high dynamics can be observed in NBT and SST50 samples with high sintering quality.

The satisfactory energy density is closely related to a high E_b value caused by a wide band gap (E_g). We give the UV–vis absorption spectra to obtain the E_g values of all the samples, as depicted in Fig. 5 (a). Increased E_g value is observed with increasing the SST content, with values ranging from 2.97 eV to 3.26 eV. With the widening of the band gap, it is more difficult for the electron to jump from the valence band to the conduction band, which is conducive to the enhancement of the intrinsic breakdown strength [32]. The monotonically increasing E_b value can be found in the inset of Fig. 5 (a), which is also associated with the decrease in the average grain size of ceramics, as mentioned earlier. Furthermore, Weibull distribution are represented in Fig. 5 (b), the slope β values of more than 20 can be observed for modified NBT ceramics, which proves the high reliability of the sample quality [33].

To evaluate the ESP of the (1-*x*)NBT-*x*SST samples, the unipolar *P-E* hysteresis loops under the critical electric field at room temperature and 10 Hz were measured and presented in Fig. 5 (c). We can see that the remnant polarization sharply decreases with increasing SST concentration, reaching the value of 1.48 μC·cm^{-2} at $x = 0.50$ mol. Benefiting from the enhanced E_b and suppressed P_r, excellent ESP can be expected in the (1-*x*)NBT-*x*SST systems. Fig. 4 (d) depicts the energy storage parameters (W_{rec} and η) of ceramics with different SST contents. Obviously, the composition of SST50 possesses an ultrahigh W_{rec} of 5.02 J·cm^{-3} under an electric field of 422 kV·cm^{-1}, accompanied by a high η of ~ 90%. Furthermore, a comparison of W_{rec} and corresponding η values among recently reported bulk ceramics are presented in Fig. 5 (e). [10,12,14,16,18,21,22,26,27,34–59] As seen, a great deal of work has been done on the exploration of high-performance lead-free ceramics. And a high W_{rec} is often achieved at the expense of η, and vice versa. Fortunately, the SST50 ceramics we designed in this work exhibit excellent comprehensive ESP characterized by an ultrahigh W_{rec} of 5.02 J·cm^{-3} and a high η of ~ 90% synchronously, outperform those of other bulk ceramics.

From application viewpoint, good stability of energy storage devices operating at elevated temperature is also essential. Fig. 6 (a) shows the temperature dependent the *P-E* loop for the optimized composition of $x = 0.50$ at 250 kV·cm^{-1} within the temperature range of 20 °C-180 °C. The corresponding W_{rec} and η values under different temperatures are calculated and summarized in Fig. 6 (b). It should be noted here that although the increased P_r and decreased P_{max} with increasing temperature can be detected, the W_{rec} and η values fluctuate very little over the whole test temperature range, with values ranging from 2.77 J·cm^{-3} (20 °C) to 2.16 J·cm^{-3} (180 °C) and from 92.67% (20 °C) to 83.46% (180 °C), respectively. Moreover, temperature stability of recently reported representative lead-free ceramics are summarized in Fig. 6 (c). [7,16,18,22,26,28,35,45,49,50,55,58,60] It is still a challenging task to develop dielectric ceramics simultaneously with large W_{rec} and temperature stability. By contrast, SST50 ceramics perform better than other lead-free ceramics both in terms of a higher W_{rec} and a wider working temperature range. These results provide solid evidence for the temperature-insensitive ESP of SST50 ceramics. Similarly, the frequency dependence of the *P-E* loop for the SST50 ceramics at 250 kV·cm^{-1} was further measured, as presented in Fig. S5 (a). Apparently, SST50 ceramics always maintain a low hysteresis behavior at 1 Hz-100 Hz.

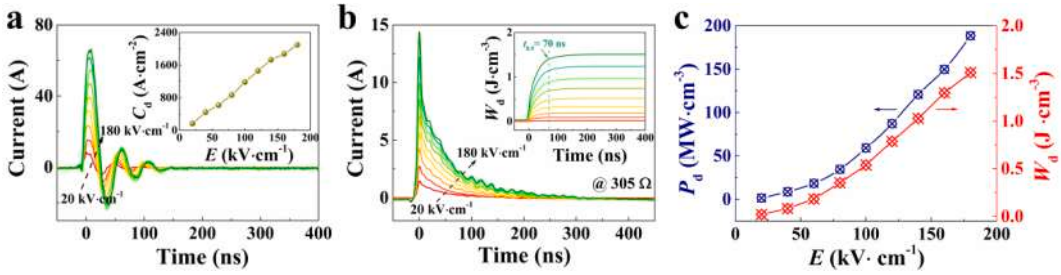

Fig. 7. (a) Under-damped discharge waveforms of the SST50 ceramics at various electric fields. Inset is the corresponding C_d value. (b) Over-damped discharging waveforms of the SST50 ceramics at various electric fields. Inset shows the variation of discharge energy density with time. (c) P_d and W_d values of the SST50 ceramic at various electric fields.

Although the P_{max} value slightly decreases and the P_r value gradually increases with the increase of frequency, outstanding frequency stability with the variation of $W_{rec} < 5\%$ and the variation of $\eta < 3\%$ at all the tested frequencies (Fig. S5 (b)) is realized in SST50 solid solution.

In practical applications, dielectric capacitors are required to possess fast discharging rate and large power density. Therefore, we test the discharge behavior of SST50 ceramics as depicted in Fig. 7. Fig. 7 (a) gives under-damped discharge waveforms of the SST50 ceramic at various electric fields. The peak value of current (I_{max}) increases rapidly with increasing electric field and the corresponding value of current density (C_d) is also increasing due to the formula ($C_d = I_{max}/S$, where S means electrode area of 3.14 mm^2), as shown in the inset. Furthermore, the values of power density (P_d, $P_d = \frac{I_{max} \times E}{2S}$) can be calculated and summarized in Fig. 7 (c). One can see that the P_d value is as high as 188.6 MW·cm^{-3} under an applied electric field of 180 kV·cm^{-1}. Over-damped discharging waveforms of the SST50 ceramics at various electric fields are given in Fig. 7 (b) and the inset displays the variation of discharge energy density (W_d, $W_d = R\int I^2 t dt/V$) with time. Obviously, W_d reaches its maximum quickly in a short time, and only 69 ns is needed to release 90% of all energy ($t_{0.9}$ = 69 ns), which proves the extremely fast discharge rate of the sample. As a result, an ultrahigh P_d of 188.6 MW·cm^{-3}, an extremely transient $t_{0.9}$ of 70 ns and a high W_d of 1.5 J·cm^{-3} can be simultaneously achieved in SST50 ceramics under 180 kV·cm^{-1}.

3. Conclusions

In summary, the (1-x)NBT-xSST ceramics were successfully prepared by solid-state reaction method for energy storage capacitors based on multi-scale optimization strategy. The increased band gaps and decreased grain size can be detected, thanks to the introduction of SST, which are all together contribute to the noteworthy enhancement of E_b and W_{rec}. Furthermore, the substitution of SST greatly induces highly dynamic PNRs with smaller size and improves the RFE properties, which is responsible for increased η. Consequently, the SST50 ceramics designed in this work possess superior comprehensive ESP characterized by an ultrahigh W_{rec} of 5.02 J·cm^{-3} and a giant η of ~ 90% under 422 kV·cm^{-1}, accompanied by excellent temperature stability (20 °C-180 °C) at 250 kV·cm^{-1}. More importantly, it is worth noting that the W_{rec} values would be further enhanced in corresponding MLCC due to the greatly improved E_b. In addition, outstanding discharge characteristics (P_d = 188.6 MW·cm^{-3}, $t_{0.9}$ = 70 ns) can also be obtained in the optimized composition of x = 0.50 mol. All the merits demonstrate that the SST50 lead-free RFE ceramics can be considered as promising dielectrics for next-generation energy storage capacitors.

Declaration of Competing Interest

The authors declare that they have no known competing financial interests or personal relationships that could have appeared to influence the work reported in this paper.

Acknowledgments

This work was supported by the National Key Research and Development Program of China (Grant 2017YFB0406301), the National Natural Science Foundation of China (51972260, 52072295), the Fundamental Research Funds for the Central University, and the 111 Project of China (B14040). The SEM work was done at the International Center for Dielectric Research (ICDR), Xi'an Jiaotong University, Xi'an, China.

Appendix A. Supplementary data

Supplementary data to this article can be found online at https://doi.org/10.1016/j.cej.2021.129601.

References

[1] Z. Yao, Z. Song, H. Hao, Z. Yu, M. Cao, S. Zhang, M.T. Lanagan, H. Liu, Homogeneous/inhomogeneous-structured dielectrics and their energy-storage performances, Adv. Mater. 29 (20) (2017) 1601727.
[2] D. Wang, Z. Fan, W. Li, D.i. Zhou, A. Feteira, G.e. Wang, S. Murakami, S. Sun, Q. Zhao, X. Tan, I.M. Reaney, High energy storage density and large strain in Bi$(Zn_{2/3}Nb_{1/3})O_3$-doped $BiFeO_3$-$BaTiO_3$ ceramics, ACS Appl. Energy Mater. 1 (8) (2018) 4403–4412.
[3] P.-J. Wang, D. Zhou, J. Li, L.-X. Pang, W.-F. Liu, J.-Z. Su, C. Singh, S. Trukhanov, A. Trukhanov, Significantly enhanced electrostatic energy storage performance of P(VDF-HFP)/$BaTiO_3$-Bi$(Li_{0.5}Nb_{0.5})O_3$ nanocomposites, Nano Energy 78 (2020), 105247.
[4] F. Yan, K. Huang, T. Jiang, X. Zhou, Y. Shi, G. Ge, B.o. Shen, J. Zhai, Significantly enhanced energy storage density and efficiency of BNT-based perovskite ceramics via A-site defect engineering, Energy Storage Mater. 30 (2020) 392–400.
[5] P.-J. Wang, D.i. Zhou, H.-H. Guo, W.-F. Liu, J.-Z. Su, M.-S. Fu, C. Singh, S. Trukhanov, A. Trukhanov, Ultrahigh enhancement rate of the energy density of flexible polymer nanocomposites using core-shell $BaTiO_3$@MgO structures as the filler, J. Mater. Chem. A 8 (22) (2020) 11124–11132.
[6] Z. Lu, G.e. Wang, W. Bao, J. Li, L. Li, A. Mostaed, H. Yang, H. Ji, D. Li, A. Feteira, F. Xu, D.C. Sinclair, D. Wang, S.-Y. Liu, I.M. Reaney, Superior energy density through tailored dopant strategies in multilayer ceramic capacitors, Energy Environ. Sci. 13 (9) (2020) 2938–2948.
[7] S. Li, T. Hu, H. Nie, Z. Fu, C. Xu, F. Xu, G. Wang, X. Dong, Giant energy density and high efficiency achieved in silver niobate-based lead-free antiferroelectric ceramic capacitors via domain engineering, Energy Storage Mater. 34 (2021) 417–426.
[8] Q.i. Li, F.-Z. Yao, Y. Liu, G. Zhang, H. Wang, Q. Wang, High-temperature dielectric materials for electrical energy storage, Annu. Rev. Mater. Res. 48 (1) (2018) 219–243.
[9] G. Ge, K. Huang, S. Wu, F. Yan, X. Li, B.o. Shen, J. Zhai, Synergistic optimization of antiferroelectric ceramics with superior energy storage properties via phase structure engineering, Energy Storage Mater. 35 (2021) 114–121.
[10] L. Zhang, Y. Pu, M. Chen, T. Wei, X. Peng, Novel $Na_{0.5}Bi_{0.5}Ti_{0.5}O_3$ based, lead-free energy storage ceramics with high power and energy density and excellent high-temperature stability, Chem. Eng. J. 383 (2020), 123154.
[11] X. Qiao, D.i. Wu, F. Zhang, B.i. Chen, X. Ren, P. Liang, H. Du, X. Chao, Z. Yang, $Bi_{0.5}Na_{0.5}TiO_3$-based relaxor ferroelectric ceramic with large energy density and high efficiency under a moderate electric field, J. Mater. Chem. C 7 (34) (2019) 10514–10520.
[12] X. Qiao, A. Sheng, D.i. Wu, F. Zhang, B.i. Chen, P. Liang, J. Wang, X. Chao, Z. Yang, A novel multifunctional ceramic with photoluminescence and outstanding energy storage properties, Chem. Eng. J. 408 (2021) 127368, https://doi.org/10.1016/j.cej.2020.127368.
[13] T. Shao, H. Du, H. Ma, S. Qu, J. Wang, J. Wang, X. Wei, Z. Xu, Potassium-sodium niobate based lead-free ceramics: novel electrical energy storage materials, J. Mater. Chem. A 5 (2) (2017) 554–563.

[14] Z. Yang, F. Gao, H. Du, L.i. Jin, L. Yan, Q. Hu, Y. Yu, S. Qu, X. Wei, Z. Xu, Y.-J. Wang, Grain size engineered lead-free ceramics with both large energy storage density and ultrahigh mechanical properties, Nano Energy 58 (2019) 768–777.

[15] R. Waser, TrI4: The role of grain boundaries in conduction and breakdown of perovskite-type titanates, Ferroelectrics 133 (1) (1992) 109–114.

[16] Z. Yang, H. Du, L.i. Jin, Q. Hu, H.e. Wang, Y. Li, J. Wang, F. Gao, S. Qu, Realizing high comprehensive energy storage performance in lead-free bulk ceramics via designing an unmatched temperature range, J. Mater. Chem. A 7 (48) (2019) 27256–27266.

[17] Y. Wu, Y. Fan, N. Liu, P. Peng, M. Zhou, S. Yan, F. Cao, X. Dong, G. Wang, Enhanced energy storage properties in sodium bismuth titanate-based ceramics for dielectric capacitor applications, J. Mater. Chem. C 7 (21) (2019) 6222–6230.

[18] Z. Pan, D.i. Hu, Y. Zhang, J. Liu, B.o. Shen, J. Zhai, Achieving high discharge energy density and efficiency with NBT-based ceramics for application in capacitors, J. Mater. Chem. C 7 (14) (2019) 4072–4078.

[19] D.a. Li, Y. Lin, Q. Yuan, M. Zhang, L. Ma, H. Yang, A novel lead-free $Na_{0.5}Bi_{0.5}TiO_3$-based ceramic with superior comprehensive energy storage and discharge properties for dielectric capacitor applications, J. Materiomics 6 (4) (2020) 743–750.

[20] J. Li, F. Li, Z. Xu, S. Zhang, Multilayer lead-free ceramic capacitors with ultrahigh energy density and efficiency, Adv. Mater. 30 (32) (2018) 1802155.

[21] Q. Yuan, F.-Z. Yao, S.-D. Cheng, L. Wang, Y. Wang, S.-B. Mi, Q. Wang, X. Wang, H. Wang, Bioinspired hierarchically structured all-inorganic nanocomposites with significantly improved capacitive performance, Adv. Funct. Mater. 30 (23) (2020) 2000191.

[22] Q. Yuan, G.-L.-F.-Z. Yao, S.-D. Cheng, Y. Wang, R. Ma, S.-B. Mi, M. Gu, K. Wang, J.-F. Li, H. Wang, Simultaneously achieved temperature-insensitive high energy density and efficiency in domain engineered $BaTiO_3$-$Bi(Mg_{0.5}Zr_{0.5})O_3$ lead-free relaxor ferroelectrics, Nano Energy 52 (2018) 203–210.

[23] H. Pan, J. Ma, J. Ma, Q. Zhang, X. Liu, B. Guan, L. Gu, X. Zhang, Y.-J. Zhang, L. Li, Y. Shen, Y.-H. Lin, C.-W. Nan, Giant energy density and high efficiency achieved in bismuth ferrite-based film capacitors via domain engineering, Nat. Commun. 9 (2018) 1813.

[24] F.-Z. Yao, M.-H. Zhang, K. Wang, J.-J. Zhou, F. Chen, B. Xu, F. Li, Y. Shen, Q.-H. Zhang, L. Gu, X.-W. Zhang, J.-F. Li, Refreshing piezoelectrics: distinctive role of manganese in lead-free perovskites, ACS Appl. Mater. Interfaces 10 (43) (2018) 37298–37306.

[25] T. Zheng, H. Wu, Y. Yuan, X. Lv, Q. Li, T. Men, C. Zhao, D. Xiao, J. Wu, K. Wang, J.-F. Li, Y. Gu, J. Zhu, S.J. Pennycook, Structural origin of enhanced piezoelectric performance and stability in lead free ceramics, Energy Environ. Sci. 10 (2017) 528–537.

[26] Y. Lin, D. Li, M. Zhang, S. Zhan, Y. Yang, H. Yang, Q. Yuan, Excellent energy-storage properties achieved in $BaTiO_3$-based lead-free relaxor ferroelectric ceramics via domain engineering on the nanoscale, ACS Appl. Mater. Interfaces 11 (40) (2019) 36824–36830.

[27] X. Ren, L. Jin, Z. Peng, B. Chen, X. Qiao, D. Wu, G. Li, H. Du, Z. Yang, X. Chao, Regulation of energy density and efficiency in transparent ceramics by grain refinement, Chem. Eng. J. 390 (2020), 124566.

[28] N. Qu, H. Du, X. Hao, A new strategy to realize high comprehensive energy storage properties in lead-free bulk ceramics, J. Mater. Chem. C 7 (26) (2019) 7993–8002.

[29] X. Liu, X. Tan, Giant strains in non-textured $(Bi_{1/2}Na_{1/2})TiO_3$-based lead-free ceramics, Adv. Mater. 28 (3) (2016) 574–578.

[30] T. Li, X. Lou, X. Ke, S. Cheng, S. Mi, X. Wang, J. Shi, X. Liu, G. Dong, H. Fan, Y. Wang, X. Tan, Giant strain with low hysteresis in A-site-deficient $(Bi_{0.5}Na_{0.5})TiO_3$-based lead-free piezoceramics, Acta Mater. 128 (2017) 337–344.

[31] P. Shi, T. Li, X. Luo, Z. Yu, X. Zhu, C. Zhou, Q. Liu, L. He, X. Zhang, S. Yang, Large electric-field-induced strain and energy storage properties in $Bi_{0.5}Na_{0.5}TiO_3$-$(0.5Ba_{0.7}Ca_{0.3}TiO_3$-$0.5BaTi_{0.8}Zr_{0.2}O_3)$ lead-free relaxor ferroelectric ceramics, J. Alloy. Compd. 860 (2021), 158369.

[32] N. Luo, K. Han, M.J. Cabral, X. Liao, S. Zhang, C. Liao, G. Zhang, X. Chen, Q. Feng, J.-F. Li, Y. Wei, Constructing phase boundary in $AgNbO_3$ antiferroelectrics: pathway simultaneously achieving high energy density and efficiency, Nat. Commun. 11 (2020) 4824.

[33] H. Qi, R. Zuo, A. Xie, A. Tian, J. Fu, Y. Zhang, S. Zhang, Ultrahigh energy-storage density in $NaNbO_3$-based lead-free relaxor antiferroelectric ceramics with nanoscale domains, Adv. Funct. Mater. 29 (2019) 1903877.

[34] Q. Hu, Y. Tian, Q. Zhu, J. Bian, L. Jin, H. Du, D.O. Alikin, V.Y. Shur, Y. Feng, Z. Xu, X. Wei, Achieve ultrahigh energy storage performance in $BaTiO_3$-$Bi(Mg_{1/2}Ti_{1/2})O_3$ relaxor ferroelectric ceramics via nano-scale polarization mismatch and reconstruction, Nano Energy 67 (2020), 104264.

[35] D. Li, Y. Lin, M. Zhang, H. Yang, Achieved ultrahigh energy storage properties and outstanding charge–discharge performances in $(Na_{0.5}Bi_{0.5})_{0.7}Sr_{0.3}TiO_3$-based ceramics by introducing a linear additive, Chem. Eng. J. 392 (2019), 123729.

[36] N. Luo, K. Han, F. Zhuo, C. Xu, G. Zhang, L. Liu, X. Chen, C. Hu, H. Zhou, Y. Wei, Aliovalent A-site engineered $AgNbO_3$ lead-free antiferroelectric ceramics toward superior energy storage density, J. Mater. Chem. A 7 (23) (2019) 14118–14128.

[37] N. Luo, K. Han, F. Zhuo, L. Liu, X. Chen, B. Peng, X. Wang, Q. Feng, Y. Wei, Design for high energy storage density and temperature-insensitive lead-free antiferroelectric ceramics, J. Mater. Chem. C 7 (17) (2019) 4999–5008.

[38] Z. Dai, J. Xie, W. Liu, X. Wang, L. Zhang, Z. Zhou, J. Li, X. Ren, Effective strategy to achieve excellent energy storage properties in lead-free $BaTiO_3$-based bulk ceramics, ACS Appl. Mate, Interfaces 12 (27) (2020) 30289–30296.

[39] T. Li, P. Chen, F. Li, C. Wang, Energy storage performance of $Na_{0.5}Bi_{0.5}TiO_3$-$SrTiO_3$ lead-free relaxors modified by $AgNb_{0.85}Ta_{0.15}O_3$, Chem. Eng. J. 406 (2021), 127151.

[40] W. Wang, Y. Pu, X. Guo, R. Shi, M. Yang, J. Li, Enhanced energy storage and fast charge-discharge capability in $Ca_{0.5}Sr_{0.5}TiO_3$-based linear dielectric ceramic, J. Alloy. Compd. 817 (2020), 152695.

[41] L. Yang, X. Kong, Z. Cheng, S. Zhang, Enhanced energy storage performance of sodium niobate based relaxor dielectrics by ramp-to-spike sintering profile, ACS Appl. Mate. Interfaces 12 (2020) 32834–32841.

[42] Z. Dai, J. Xie, X. Fan, X. Ding, W. Liu, S. Zhou, X. Ren, Enhanced energy storage properties and stability of $Sr(Sc_{0.5}Nb_{0.5})O_3$ modified $0.65BaTiO_3$-$0.35Bi_{0.5}Na_{0.5}TiO_3$ ceramics, Chem. Eng. J. 397 (2020), 125520.

[43] Y. Pu, W. Wang, X. Guo, R. Shi, M. Yang, J. Li, Enhancing the energy storage properties of $Ca_{0.5}Sr_{0.5}TiO_3$-based lead-free linear dielectric ceramics with excellent stability through regulating grain boundary defects, J. Mater. Chem. C 7 (45) (2019) 14384–14393.

[44] Z. Cai, C. Zhu, H. Wang, P. Zhao, Y. Yu, L. Li, X. Wang, Giant dielectric breakdown strength together with ultrahigh energy density in ferroelectric bulk ceramics via layer-by-layer engineering, J. Mater. Chem. A 7 (29) (2019) 17283–17291.

[45] M. Zhang, H. Yang, D. Li, L. Ma, Y. Lin, Giant energy storage efficiency and high recoverable energy storage density achieved in $K_{0.5}Na_{0.5}NbO_3$-$Bi(Zn_{0.5}Zr_{0.5})O_3$ ceramics, J. Mater. Chem. C 8 (26) (2020) 8777–8785.

[46] J. Gao, Q. Liu, J. Dong, X. Wang, S. Zhang, J.-F. Li, Local structure heterogeneity in Sm-doped $AgNbO_3$ for improved energy storage performance, ACS Appl. Mater. Interfaces 12 (5) (2020) 6097–6104.

[47] Y. Huang, C. Zhao, B. Wu, J. Wu, Multifunctional $BaTiO_3$-based relaxor ferroelectrics toward excellent energy storage performance and electrostrictive strain benefiting from crossover region, ACS Appl. Mater. Interfaces 12 (21) (2020) 23885–23895.

[48] Y. Lin, D. Li, M. Zhang, H. Yang, $(Na_{0.5}Bi_{0.5})_{0.7}Sr_{0.3}TiO_3$ modified by $Bi(Mg_{2/3}Nb_{1/3})O_3$ ceramics with high energy-storage properties and an ultrafast discharge rate, J. Mater. Chem. C 8 (7) (2020) 2258–2264.

[49] W.-B. Li, D. Zhou, L.-X. Pang, R. Xu, H.-H. Guo, Novel barium titanate based capacitors with high energy density and fast discharge performance, J. Mater. Chem. A 5 (37) (2017) 19607–19612.

[50] M. Zhou, R. Liang, Z. Zhou, S. Yan, X. Dong, Novel sodium niobate-based lead-free ceramics as new environment-friendly energy storage materials with high energy density, high power density, and excellent stability, ACS Sustain. Chem. Eng. 6 (10) (2018) 12755–12765.

[51] F. Yan, Y. Shi, X. Zhou, K. Zhu, B. Shen, J. Zhai, Optimization of polarization and electric field of bismuth ferrite-based ceramics for capacitor applications, Chem. Eng. J. (2020) 127945.

[52] J. Shi, X. Chen, X. Li, J. Sun, C. Sun, F. Pang, H. Zhou, Realizing ultrahigh recoverable energy density and superior charge-discharge performance in $NaNbO_3$-based lead-free ceramics via a local random field strategy, J. Mater. Chem. C 8 (11) (2020) 3784–3794.

[53] L. Zhao, J. Gao, Q. Liu, S. Zhang, J.-F. Li, Silver niobate lead-free antiferroelectric ceramics: enhancing energy storage density by B-Site doping, ACS Appl. Mate, Interfaces 10 (2018) 819–826.

[54] X. Qiao, F. Zang, D. Wu, B. Chen, X. Zhao, Z. Peng, X. Ren, P. Liang, X. Chao, Z. Yang, Superior comprehensive energy storage properties in $Bi_{0.5}Na_{0.5}TiO_3$-based relaxor ferroelectric ceramics, Chem. Eng. J. 388 (2020), 124158.

[55] M. Zhou, R. Liang, Z. Zhou, X. Dong, Superior energy storage properties and excellent stability of novel $NaNbO_3$-based lead-free ceramics with A-site vacancy obtained via a Bi_2O_3 substitution strategy, J. Mater. Chem. A 6 (37) (2018) 17896–17904.

[56] X. Zhou, H. Qi, Z. Yan, G. Xue, H. Luo, D. Zhang, Superior thermal stability of high energy density and power density in domain-engineered $Bi_{0.5}Na_{0.5}TiO_3$-$NaTaO_3$ relaxor ferroelectrics, ACS Appl. Mate, Interfaces 11 (46) (2019) 43107–43115.

[57] G. Liu, Y. Li, B. Guo, M. Tang, Q. Li, J. Dong, L. Yu, K. Yu, Y. Yan, D. Wang, L. Zhang, H. Zhang, Z. He, L. Jin, Ultrahigh dielectric breakdown strength and excellent energy storage performance in lead-free barium titanate-based relaxor ferroelectric ceramics via a combined strategy of composition modification, viscous polymer processing, and liquid-phase sintering, Chem. Eng. J. 398 (2020), 125625.

[58] G. Wang, J. Li, X. Zhang, Z. Fan, F. Yang, A. Feteira, D. Zhou, D.C. Sinclair, T. Ma, X. Tan, D. Wang, I.M. Reaney, Ultrahigh energy storage density lead-free multilayers by controlled electrical homogeneity, Energy Environ. Sci. 12 (2) (2019) 582–588.

[59] K. Han, N. Luo, S. Mao, F. Zhuo, L. Liu, B. Peng, X. Chen, C. Hu, H. Zhou, Y. Wei, Ultrahigh energy-storage density in A-/B-site codoped $AgNbO_3$ lead-free antiferroelectric ceramics: insight into the origin of antiferroelectricity, J. Mater. Chem. A 7 (2019) 26293–26301.

[60] J. Huang, H. Qi, Y. Gao, A. Xie, Y. Zhang, Y. Li, S. Wang, R. Zuo, Expanded linear polarization response and excellent energy-storage properties in $(Bi_{0.5}Na_{0.5})TiO_3$-$KNbO_3$ relaxor antiferroelectrics with medium permittivity, Chem. Eng. J. 398 (2020), 125639.